

This is an Open Access document downloaded from ORCA, Cardiff University's institutional repository: <https://orca.cardiff.ac.uk/id/eprint/141639/>

This is the author's version of a work that was submitted to / accepted for publication.

Citation for final published version:

Mikhaylov, Roman, Stringer Martin, Mercedes, Dumcius, Povilas, Wang, Hanlin, Wu, Fangda, Zhang, Xiaoyan, Alghamdi, Fahad, Akhimien, Victory, Sun, Chao, Clayton, Aled, Fu, Yong Qing (Richard), Ye, Lin, Dong, Zhiqiang and Yang, Xin 2021. A reconfigurable and portable acoustofluidic system based on flexible printed circuit board for the manipulation of microspheres. *Journal of Micromechanics and Microengineering* 31 (7), 074003. 10.1088/1361-6439/ac0515

Publishers page: <http://dx.doi.org/10.1088/1361-6439/ac0515>

Please note:

Changes made as a result of publishing processes such as copy-editing, formatting and page numbers may not be reflected in this version. For the definitive version of this publication, please refer to the published source. You are advised to consult the publisher's version if you wish to cite this paper.

This version is being made available in accordance with publisher policies. See <http://orca.cf.ac.uk/policies.html> for usage policies. Copyright and moral rights for publications made available in ORCA are retained by the copyright holders.



ACCEPTED MANUSCRIPT • OPEN ACCESS

A Reconfigurable and Portable Acoustofluidic System Based on Flexible Printed Circuit Board for the Manipulation of Microspheres

To cite this article before publication: Roman Mikhaylov *et al* 2021 *J. Micromech. Microeng.* in press <https://doi.org/10.1088/1361-6439/ac0515>

Manuscript version: Accepted Manuscript

Accepted Manuscript is “the version of the article accepted for publication including all changes made as a result of the peer review process, and which may also include the addition to the article by IOP Publishing of a header, an article ID, a cover sheet and/or an ‘Accepted Manuscript’ watermark, but excluding any other editing, typesetting or other changes made by IOP Publishing and/or its licensors”

This Accepted Manuscript is © 2021 The Author(s). Published by IOP Publishing Ltd..

As the Version of Record of this article is going to be / has been published on a gold open access basis under a CC BY 3.0 licence, this Accepted Manuscript is available for reuse under a CC BY 3.0 licence immediately.

Everyone is permitted to use all or part of the original content in this article, provided that they adhere to all the terms of the licence <https://creativecommons.org/licenses/by/3.0>

Although reasonable endeavours have been taken to obtain all necessary permissions from third parties to include their copyrighted content within this article, their full citation and copyright line may not be present in this Accepted Manuscript version. Before using any content from this article, please refer to the Version of Record on IOPscience once published for full citation and copyright details, as permissions may be required. All third party content is fully copyright protected and is not published on a gold open access basis under a CC BY licence, unless that is specifically stated in the figure caption in the Version of Record.

View the [article online](#) for updates and enhancements.

1
2
3
4
5
6
7
8
9
10
11
12
13
14
15
16
17
18
19
20
21
22
23
24
25
26
27
28
29
30
31
32
33
34
35
36
37
38
39
40
41
42
43
44

1 A Reconfigurable and Portable Acoustofluidic System Based on Flexible 2 Printed Circuit Board for the Manipulation of Microspheres

3 Roman Mikhaylov¹, Mercedes Stringer Martin¹, Povilas Dumcius¹, Hanlin Wang¹, Fangda Wu¹,
4 Xiaoyan Zhang², Fahad Alghamdi¹, Victory Akhimien¹, Chao Sun³, Aled Clayton⁴, Yongqing Fu⁵,
5 Lin Ye⁶, Zhiqiang Dong⁷, and Xin Yang¹

6 ¹ Department of Electrical and Electronic Engineering, School of Engineering, Cardiff
7 University, Cardiff CF24 3AA, UK

8 ² International Joint Laboratory of Biomedicine and Engineering, Huazhong Agricultural
9 University and Cardiff University, Wuhan, Hubei, 430070, China

10 ³ School of Life Sciences, Northwestern Polytechnical University, 710072, P.R. China

11 ⁴ Tissue Micro-Environment Group, Division of Cancer & Genetics, School of Medicine,
12 Cardiff University, Cardiff CF14 4XN, UK

13 ⁵ Faculty of Engineering and Environment, Northumbria University, Newcastle Upon Tyne,
14 Newcastle NE1 8ST, UK

15 ⁶ Cardiff China Medical Research Collaborative, Division of Cancer & Genetics, Cardiff
16 University School of Medicine, Cardiff, CF14 4XN, UK

17 ⁷ College of Biomedicine and Health, College of Life Science and Technology, Huazhong
18 Agricultural University, Wuhan, Hubei, 430070, China

44 Corresponding author: Xin Yang

45 Abstract

46 Acoustofluidic devices based on surface acoustic waves (SAWs) have been widely applied in
47 biomedical research for the manipulation and separation of cells. In this work, we develop an
48 accessible manufacturing process to fabricate an acoustofluidic device consisting of a SAW
49 interdigital transducer (IDT) and a polydimethylsiloxane (PDMS) microchannel. The IDT is
50 manufactured using a flexible printed circuit board (FPCB) pre-patterned with interdigital
51 electrodes (IDEs) that is mechanically coupled with a piezoelectric substrate. A new microchannel
52 moulding technique is realised by 3D printing on glass slides and is demonstrated by constructing
53 the microchannel for the acoustofluidic device. The flexible clamping mechanism, used to
54 construct the device, allows the reconfigurable binding between the IDT and the microchannel.
55 This unique construction makes the acoustofluidic device capable of adjusting the angle between
56 the microchannel and the SAW propagation, without refabrication, via either rotating the IDT or
57 the microchannel. The angle adjustment is demonstrated by setting the polystyrene microsphere
58 aggregation angle to -5° , 0° , 6° , and 15° . Acoustic energy density measurements demonstrate the
59 velocity of microsphere aggregation in the device can be accurately controlled by the input power.
60 The manufacturing process has the advantages of reconfigurability and rapid-prototyping to
61 facilitate preparing acoustofluidic devices for wider applications.

62 Introduction

63 Acoustofluidic devices have attracted great interest in label-free manipulations of micro-¹ and
64 nano- particles² owing to their considerable biocompatibility and precision. They have been
65 demonstrated in biomedical applications for separation (exosomes³⁻⁵, tumour⁶, and inflammatory⁷
66 cells), manipulation (cell interaction⁸, single cells⁹, and *Caenorhabditis elegans*¹⁰), and stimulation
67 of cells¹¹.

68 Surface acoustic wave (SAW) devices are almost independent from the microchannel material
69 in terms of acoustic properties compared to bulk acoustic wave devices¹². This feature makes them
70 easy to fabricate for high-frequency applications (MHz-GHz)^{3,13} and integrate with other systems,
71 such as microfluidics. SAW devices are conventionally fabricated by patterning interdigital
72 transducers (IDTs) on a piezoelectric substrate¹⁴, which convert radio frequency (RF) signals into
73 SAWs propagating on the surface of the substrate. When the SAW meets a liquid medium, it
74 diffracts into the medium and generates a time-averaged pressure distribution that can be utilised
75 to precisely manipulate micro-objects¹⁵. Standing SAW (SSAW) devices, constructed by a pair of
76 opposite IDTs working on the same frequency, are primarily used in acoustofluidic applications¹⁶.
77 A great diversity of manipulation and actuation can be achieved by setting up the IDT structure to
78 create, for example, tilted-angle SSAW devices^{17,18} and 2D- and 3D-patterning tweezers^{8,19-21}.
79 However, IDTs manufactured through conventional techniques, such as photolithography, are
80 permanently patterned on the piezoelectric substrate. Polydimethylsiloxane (PDMS)
81 microchannels, used to accommodate biological samples in acoustofluidic systems, also use the
82 photolithography process involving cleanroom facilities. Thus, acoustofluidic devices capable of
83 manufacturing and reconfiguring in general laboratories, using off-the-shelf components, are
84 highly desired.

85 A new fabrication technique, developed by our group, has successfully fabricated the IDTs
86 without the use of a cleanroom for the manipulation of microparticles and cancer cells²². The IDTs
87 were manufactured by mechanically clamping a rigid printed circuit board (PCB) pre-patterned
88 with interdigital electrodes (IDEs) onto a piezoelectric substrate. This technique has been

89 benchmarked against a device made by conventional photolithography in terms of frequency
90 response, droplet transportation, and cell manipulation. The PCB-based IDT has the advantage of
91 replacing piezoelectric substrates by simply disassembling the mechanically clamped structure,
92 with no need to remanufacture the IDT. Another IDT made by flexible PCB (FPCB) pre-patterned
93 with IDEs demonstrated similar performance with advantages of dynamic flexing, less weight, and
94 better heat dissipation²³.

95 A development process with low requirement on facilities and operation of the device using a
96 portable control unit can better support broadening the use of the acoustofluidic devices. Herein,
97 we present a novel development technique for both the IDTs and the microchannel, we call it
98 Versatile Acoustofluidic Device (VAD). We also demonstrate the rapid-prototyping and
99 reconfigurability of VAD for precise manipulation of micro-objects.

100 **Methods and Materials**

101 **FPCBs**

102 The FPCB pre-patterned with IDEs, used in the VAD, was externally manufactured
103 (circuitfly.com) using a standard PCB manufacturing process. The IDEs were made of metal
104 bilayers (Au/Ni, 30 nm/2 μm) patterned on a 70 μm thick polyester laminate. The IDEs consist of
105 40 pairs of 10 mm long finger electrodes and have a centre-to-centre finger pitch of 200 μm as
106 shown in Fig. 1A. The ratio between the finger spacing and finger width is 1:1. A 128° Y-cut 3-
107 inch lithium niobate (LiNbO_3) was used as the piezoelectric substrate. The VAD had a Rayleigh
108 mode frequency of ~ 19.9 MHz and a 200 μm wavelength. Two coaxial cables were soldered to
109 the buspads of each FPCB IDEs. Matching networks (MNs) based on an LC circuit are used (Fig.
110 1B), which are essential in reducing the impedance mismatching between the VAD and the driving
111 power amplifiers^{22,23}.

113 **Clamping Mechanism**

114 The VAD required a mechanical jig to hold the main components together, including the FPCB
115 IDEs and LiNbO_3 substrate. As shown in Fig. 1C, the VAD uses a simple clamping mechanism
116 and consists of the following stacking order from the bottom to the top: heatsink (supports the
117 entire device and dissipates heat), temperature sensors (measure the IDT temperature), LiNbO_3
118 (produces SAWs), FPCB IDEs (convert RF to SAWs), silicon pads (evenly distribute the clamping
119 force), localised pressers (apply the clamping force), force-sensitive resistors (FSRs) (measure the
120 clamping force), FSR roofs (hold and press the FSRs), M5 screws (generate the clamping force)
121 and main holders (hold the whole structure onto the heatsink). Another structure, which consists
122 of an acrylic presser and a microchannel presser, is developed to hold the microchannel between
123 the two IDTs. The FSR roofs, localised pressers, microchannel pressers, and main holders were all
124 3D printed using a 0.4 mm nozzle and polylactic acid (PLA) filaments.

126 **The VAD Assembly**

127 The FPCB IDEs, microchannel and LiNbO_3 substrate were thoroughly cleaned using isopropyl
128 alcohol and de-ionised (DI) water, dried using a compressed air duster and checked under the
129 microscope to ensure that no fibres or dust particles were present on the parts before the final
130 assembly. All the individual components, shown in Fig. 1C, are placed on the LiNbO_3 which is
131 mounted on the heatsink. A clamping force is created by fastening the two M5 screws on top of
132 the localised pressers. A vector network analyser (VNA) is used to monitor the reflection

1
2
3 133 coefficient (S_{11}) and to confirm when the contact resistance is overcome and an optimal clamping
4 134 force is achieved^{22,23}. Fig. 1D shows the final assembled VAD with a portable control unit and an
5 135 inset to demonstrate the full assembly including the microchannel on the heatsink.
6 136

8 137 **Microchannels**

9 138 The use of a glass-bottom 3D printed mould to prepare the microchannels stands as a novelty
10 139 for microchannel manufacturing, with the development flow illustrated in Fig. 2A. (1) A glass
11 140 slide (76 mm (W) × 26 mm (L)) is placed on the 3D printer table and held in place using masking
12 141 tape. A compensatory offset is applied by using a “Z offset setting” plugin in the 3D printer
13 142 software. Glass slides with various thicknesses can be used as the glass-bottom of the mould by
14 143 adjusting the offset setting. The 3D printed mould, designed in Solidworks, is directly printed on
15 144 the glass slide, (2) removed from the 3D printer table after completion and left to cool. (3) The
16 145 glass-bottom 3D printed mould is then placed in a plastic petri dish and filled with PDMS (Sylgard
17 146 184, Farnell UK), which is prepared according to the manufacturer’s protocol. The dish is placed
18 147 onto a hot plate (SD160, Colepalmer) at a temperature of 45 °C to cure for 24 hours, which is
19 148 below the 60 °C melting temperature of the PLA. (4) The set PDMS is removed from the mould,
20 149 (5) the outer perimeter of the channel is cut and (6) a premade acrylic presser, with the dimensions
21 150 of 47 mm (L) × 15 mm (W) × 3 mm (H), is placed on top of the microchannel. (7) The
22 151 microchannel is then bolted onto the pre-assembled VAD using a microchannel presser (Fig. 2B).
23 152 (8) The M5 nuts on the far edges of the microchannel presser are fastened until resistance is felt
24 153 and (9) finally the M3 screws are screwed in to ensure even distribution of the pressing force.

25 154 The walls of the microchannel presser (Fig. 2A, step 9 and Fig. 2B) are created to resist
26 155 excessive force and prevent it from overbending. These help to keep the force evenly distributed
27 156 across the microchannel and not to over compress it. To further prevent deformation, the ratio
28 157 between the PDMS and the microchannel height was 55:1.

29 158 Two examples of the glass-bottom 3D printed moulds are shown in Fig. 2C, which are single
30 159 inlet/outlet and 3-inlet-2-outlet structures, respectively. Five 3D printed moulds were printed on
31 160 the same glass slide and measured using a microscope to determine the repeatability of the print.
32 161

33 162 **Control Unit**

34 163 To increase the portability of the acoustofluidic system and facilitate on-demand use of the
35 164 VAD, a portable control unit that includes a waveform generator, a power amplifier, a
36 165 microcontroller, sensors, a display, and a power supply is developed (Fig. 3).
37 166

38 167 **Coating and Sample Preparation**

39 168 The microchannels were all coated with 1% (w/w) bovine serum albumin solution for 10 min
40 169 and then flushed with DI water. For the microsphere test, 10 µm polystyrene microspheres (Sigma
41 170 Aldrich) were used and suspended in a 23% (v/v) glycerol and phosphate-buffered saline solution.
42 171 The microsphere suspension was injected into the microchannels through a syringe.
43 172

44 173 **IDT Alignment Setup and Analysis**

45 174 The formation of SSAW relies on the alignment of the two IDTs, which can be reflected by the
46 175 device’s insertion loss (S_{21}). The smaller the insertion loss, the better the SAW transmission from
47 176 one IDT to another. Thus, one can effectively use the VNA to estimate the IDT alignment. This is
48 177 demonstrated by connecting two IDTs to the VNA as a two-port network, as shown in Fig 4. The
49 178 test keeps one of the IDTs unmoved, as the receiving IDT, while rotating the other IDT, as the

1
2
3 179 transmitting IDT. The S_{11} of the transmitting IDT is measured during this procedure to monitor
4 180 how it changes with the rotation. Top view images of the transmitting IDT at different orientations
5 181 were captured by an overhead camera, which were then analysed using a customised MATLAB
6 182 code that extracted the angle between the two IDTs. Five reference angles, 17° , 11° , 6° , 2° , and
7 183 0° , were determined for the S_{21} readings, which were selected by finding the most observable
8 184 change in the S_{21} .

11 186 **Acoustic Energy Density Analysis**

12 187 To characterise the acoustic energy density inside the VAD, a MATLAB code adapted from
13 188 Barnkob et al²⁴ was applied to analyse the trajectory of microspheres. In short, image frames
14 189 extracted from microscope-captured movies, during the microsphere aggregation process, were
15 190 analysed for pixel intensity near the pressure node (PN) line. The last frame of each movie was
16 191 used as the maximum intensity frame. The normalised intensity and the relative intensity of each
17 192 middle-process frames were then calculated and fit into an expression using a fitting parameter.

21 193 **Results and Discussion**

22 194 **IDT Alignment**

23 195 Compared to cleanroom made SSAW devices, the VAD depended on the manual alignment of
24 196 the two IDTs to produce an accurate SSAW and form an even distribution of PN and pressure anti-
25 197 node lines. The S_{21} peak can be used to establish the angle of the IDTs, where the 0° angle achieves
26 198 the maximum S_{21} peak as shown in Fig. 5A. The S_{11} of the transmitting IDT shows a dip of -28 dB
27 199 when the two IDTs are in parallel (Fig. 5B), which is within an acceptable working range of
28 200 conventional SAW devices²⁵.

32 202 **Microchannel Characterisation**

33 203 Fig. 6A shows the average height and width of the 3D printed moulds, i.e. $102.8 \pm 11.4 \mu\text{m}$
34 204 (Mean \pm SD) and $451.4 \pm 42.6 \mu\text{m}$ (Mean \pm SD), respectively. Of which a $500 \mu\text{m}$ wide 3D printed
35 205 mould is used to produce the microchannel for the following tests (Fig. 6B). The bonding strength
36 206 of the assembled microchannel met the high throughput requirement by flushing a sample at a flow
37 207 rate of up to $6 \text{ mL}/\text{min}$ ²⁶.

40 209 **Acoustic Energy Density within the VAD**

41 210 The acoustic energy density of the VAD at 0° is registered at 15, 20 and 27 dBm input power,
42 211 as the results shown in Figs. 7A-7C, respectively. The time lapse required for 99% of microspheres
43 212 to aggregate on the PN line is ~ 1.9 , ~ 0.6 , and ~ 0.3 sec for the three input powers. The average
44 213 acoustic energy density of the powers is shown in Fig. 7D, which indicates that the acoustic
45 214 radiation force exerted on the microspheres can be fully controlled by tuning the input power.

48 216 **Rotating the IDTs to Adjust the Tilted-Angle**

49 217 The VAD can offer reconfigurable tilted-angles (angle between the PN lines and the
50 218 microchannel) without the need of fabricating new devices. The optimal tilted-angle degree in cell
51 219 separation depends on the sample flow rate, where a high tilted-angle is optimal for the flow rate
52 220 of $25 \mu\text{L}/\text{min}$ and a low tilted-angle for $50\text{-}125 \mu\text{L}/\text{min}$ ⁶. The ability of VAD to vary the tilted-
53 221 angle can potentially save considerable manufacturing effort and cost in reconfiguring devices for
54 222 versatile and flexible applications. By simply rotating one of the IDTs, we manage to configure

the PN lines orientation into two tilted-angles, 0° and 6° , illustrated by the microsphere aggregation shown in Figs. 8A and 8B, respectively. The results demonstrate the ability of the VAD in rapid reconfiguration of the tilted-angle to tackle different applications.

Visually Guided Assembly of the VAD

The VAD is tested for whether visually aligning the two opposite IDTs by eye can achieve similar performance as the VNA guided assembly. The VAD is assembled visually using the FSRs readings as reference. The alignment quality, represented by the S_{21} , is shown in Fig. 9A. Comparing with the VNA guided alignments (blue curve), the visually guided alignments (orange curve) present a smaller S_{21} . Fig. 9B shows the acoustic energy density is slightly higher in the visually guided assembly. This could be because the distance between the opposing IDTs may have been reduced during the visual experiments⁶. Since the IDTs are pushed further forward to expose their front edge and allow them to be easily visually aligned.

In addition, we collected the microsphere aggregation image for the visually guided assembly, as shown in Fig. 9C, which achieves a similar pattern as that in the VNA guided assembly (Fig. 8A). Overall, this confirms that the assembling process of the VAD can be achieved by the visual alignment of the two IDTs without the use of the VNA.

Rotating the Microchannel

The unique construction of the VAD allows an alternative way to alter the tilted-angle by rotating the microchannel clamped to the VAD. New microchannel pressers are printed with two degrees including 15° and -5° to accommodate a wider microchannel as shown in Fig. 10A. These pressers are utilised to clamp the microchannel and to create the respective inclinations for aggregating the microspheres, as shown in Fig. 10B.

It is noted that the reconfiguration of the tilted-angles can be achieved by either rotating the microchannel or the IDTs. It may be preferable to rotate the microchannel as it does not require to rotate the IDT, which may potentially affect the frequency response of the VAD.

Conclusion

This paper introduced a novel technology to manufacture the SAW-based acoustofluidic system, including both the SAW IDT and the PDMS microchannel, without the need of a cleanroom facility. It was demonstrated that a pair of FPCB IDEs were mechanically coupled to the piezoelectric substrate to produce SSAWs, under the guide of either eyes or the VNA. The VAD offers great flexibility in resetting the tilted-angle between the IDTs and the microchannel, resulting in rotatable PN lines inside the acoustofluidic device. The VAD can accomplish a rapid acoustofluidic prototyping process as an alternative to the conventional cleanroom process.

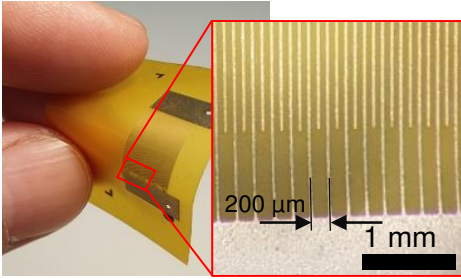
Acknowledgements

The authors would gratefully acknowledge the financial support from EPSRC (EP/P002803/1, EP/P018998/1), EPSRC IAA, Wellcome Trust, Global Challenges Research Fund (GCRF), the Royal Society (IEC\NSFC\170142, IE161019), and the Natural Science Foundation of China (NSFC) (Grant No. 51811530310).

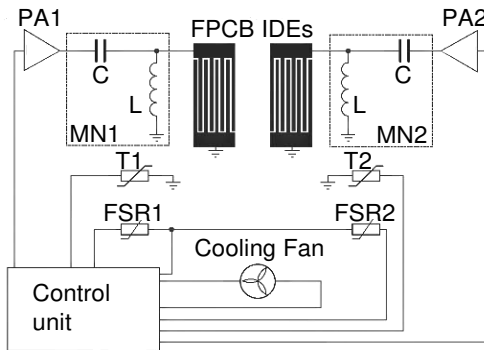
263 **References**

- 264 1 Z. Tian, S. Yang, P.-H. Huang, Z. Wang, P. Zhang, Y. Gu, H. Bachman, C. Chen, M. Wu, Y.
265 Xie and T. J. Huang, Wave number–spiral acoustic tweezers for dynamic and reconfigurable
266 manipulation of particles and cells, *Science Advances*, 2019, **5**, eaau6062.
- 267 2 M. Wu, Z. Mao, K. Chen, H. Bachman, Y. Chen, J. Rufo, L. Ren, P. Li, L. Wang and T. J.
268 Huang, Acoustic Separation of Nanoparticles in Continuous Flow, *Advanced Functional*
269 *Materials*, 2017, **27**, 1606039.
- 270 3 M. Wu, Y. Ouyang, Z. Wang, R. Zhang, P.-H. Huang, C. Chen, H. Li, P. Li, D. Quinn, M. Dao,
271 S. Suresh, Y. Sadovsky and T. J. Huang, Isolation of exosomes from whole blood by integrating
272 acoustics and microfluidics, *Proc. Natl. Acad. Sci. U.S.A.*, 2017, **114**, 10584–10589.
- 273 4 M. Wu, C. Chen, Z. Wang, H. Bachman, Y. Ouyang, P.-H. Huang, Y. Sadovsky and T. J.
274 Huang, Separating extracellular vesicles and lipoproteins via acoustofluidics, *Lab Chip*, 2019,
275 **19**, 1174–1182.
- 276 5 Y. Gu, C. Chen, Z. Mao, H. Bachman, R. Becker, J. Rufo, Z. Wang, P. Zhang, J. Mai, S. Yang,
277 J. Zhang, S. Zhao, Y. Ouyang, D. T. W. Wong, Y. Sadovsky and T. J. Huang, Acoustofluidic
278 centrifuge for nanoparticle enrichment and separation, *Science Advances*, 2021, **7**, eabc0467.
- 279 6 P. Li, Z. Mao, Z. Peng, L. Zhou, Y. Chen, P.-H. Huang, C. I. Truica, J. J. Drabick, W. S. El-
280 Deiry, M. Dao, S. Suresh and T. J. Huang, Acoustic separation of circulating tumor cells, *PNAS*,
281 2015, **112**, 4970–4975.
- 282 7 S. Li, L. Ren, P.-H. Huang, X. Yao, R. A. Cuento, J. P. McCoy, C. E. Cameron, S. J. Levine
283 and T. J. Huang, Acoustofluidic Transfer of Inflammatory Cells from Human Sputum Samples,
284 *Analytical Chemistry*, 2016, **88**, 5655–5661.
- 285 8 F. Guo, P. Li, J. B. French, Z. Mao, H. Zhao, S. Li, N. Nama, J. R. Fick, S. J. Benkovic and T.
286 J. Huang, Controlling cell–cell interactions using surface acoustic waves, *PNAS*, 2015, **112**, 43–
287 48.
- 288 9 D. Ahmed, A. Ozcelik, N. Bojanala, N. Nama, A. Upadhyay, Y. Chen, W. Hanna-Rose and T.
289 J. Huang, Rotational manipulation of single cells and organisms using acoustic waves, *Nature*
290 *Communications*, 2016, **7**, 11085.
- 291 10 J. Zhang, S. Yang, C. Chen, J. H. Hartman, P.-H. Huang, L. Wang, Z. Tian, P. Zhang, D.
292 Faulkenberry, J. N. Meyer and T. J. Huang, Surface acoustic waves enable rotational
293 manipulation of *Caenorhabditis elegans*, *Lab Chip*, 2019, **19**, 984–992.
- 294 11 L. A. Ambattu, S. Ramesan, C. Dekiwadia, E. Hanssen, H. Li and L. Y. Yeo, High frequency
295 acoustic cell stimulation promotes exosome generation regulated by a calcium-dependent
296 mechanism, *Commun Biol*, 2020, **3**, 553.
- 297 12 K. Xu, C. P. Clark, B. L. Poe, J. A. Lounsbury, J. Nilsson, T. Laurell and J. P. Landers, Isolation
298 of a Low Number of Sperm Cells from Female DNA in a Glass–PDMS–Glass Microchip via
299 Bead-Assisted Acoustic Differential Extraction, *Anal. Chem.*, 2019, **91**, 2186–2191.
- 300 13 R. J. Shilton, M. Travagliati, F. Beltram and M. Cecchini, Nanoliter-Droplet Acoustic
301 Streaming via Ultra High Frequency Surface Acoustic Waves, *Advanced Materials*, 2014, **26**,
302 4941–4946.
- 303 14 Y. Ai, C. K. Sanders and B. L. Marrone, Separation of *Escherichia coli* Bacteria from Peripheral
304 Blood Mononuclear Cells Using Standing Surface Acoustic Waves, *Anal. Chem.*, 2013, **85**,
305 9126–9134.
- 306 15 N. Nama, R. Barnkob, Z. Mao, C. J. Kähler, F. Costanzo and T. J. Huang, Numerical study of
307 acoustophoretic motion of particles in a PDMS microchannel driven by surface acoustic waves,
308 *Lab Chip*, 2015, **15**, 2700–2709.

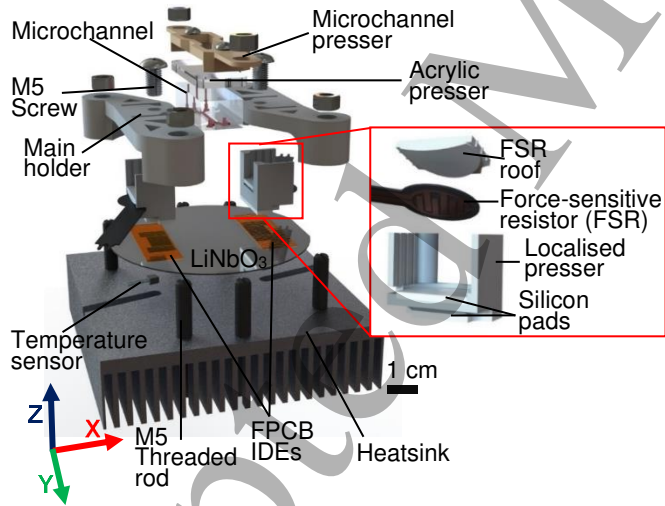
- 1
2
3 309 16A. Ozcelik, J. Rufo, F. Guo, Y. Gu, P. Li, J. Lata and T. J. Huang, Acoustic tweezers for the life
4 310 sciences, *Nature Methods*, 2018, **15**, 1021.
- 5 311 17G. Liu, F. He, Y. Li, H. Zhao, X. Li, H. Tang, Z. Li, Z. Yang and Y. Zhang, Effects of two
6 312 surface acoustic wave sorting chips on particles multi-level sorting, *Biomed Microdevices*,
7 313 2019, **21**, 59.
- 8 314 18K.-A. Hyun, H. Gwak, J. Lee, B. Kwak and H.-I. Jung, Salivary Exosome and Cell-Free DNA
9 315 for Cancer Detection, *Micromachines*, 2018, **9**, 340.
- 10 316 19Y. Wang, C. Han and D. Mei, Standing Surface Acoustic Wave-Assisted Fabrication of Region-
11 317 Selective Microstructures via User-Defined Waveguides, *Langmuir*, 2019, **35**, 11225–11231.
- 12 318 20F. Guo, Z. Mao, Y. Chen, Z. Xie, J. P. Lata, P. Li, L. Ren, J. Liu, J. Yang, M. Dao, S. Suresh
13 319 and T. J. Huang, Three-dimensional manipulation of single cells using surface acoustic waves,
14 320 *PNAS*, 2016, **113**, 1522–1527.
- 15 321 21T. D. Nguyen, V. T. Tran, Y. Q. Fu and H. Du, Patterning and manipulating microparticles into
16 322 a three-dimensional matrix using standing surface acoustic waves, *Appl. Phys. Lett.*, 2018, **112**,
17 323 213507.
- 18 324 22R. Mikhaylov, F. Wu, H. Wang, A. Clayton, C. Sun, Z. Xie, D. Liang, Y. Dong, F. Yuan, D.
19 325 Moschou, Z. Wu, M. H. Shen, J. Yang, Y. Fu, Z. Yang, C. Burton, R. J. Errington, M. Wiltshire
20 326 and X. Yang, Development and characterisation of acoustofluidic devices using detachable
21 327 electrodes made from PCB, *Lab Chip*, 2020, **20**, 1807–1814.
- 22 328 23C. Sun, R. Mikhaylov, Y. Fu, F. Wu, H. Wang, X. Yuan, Z. Xie, D. Liang, Z. Wu and X. Yang,
23 329 Flexible Printed Circuit Board as Novel Electrodes for Acoustofluidic Devices, *IEEE*
24 330 *Transactions on Electron Devices*, 2021, **68**, 393–398.
- 25 331 24R. Barnkob, I. Iranmanesh, M. Wiklund and H. Bruus, Measuring acoustic energy density in
26 332 microchannel acoustophoresis using a simple and rapid light-intensity method, *Lab on a Chip*,
27 333 2012, **12**, 2337–2344.
- 28 334 25F. Wu, M. H. Shen, J. Yang, H. Wang, R. Mikhaylov, A. Clayton, X. Qin, C. Sun, Z. Xie, M.
29 335 Cai, J. Wei, D. Liang, F. Yuan, Z. Wu, Y. Fu, Z. Yang, X. Sun, L. Tian and X. Yang, An
30 336 Enhanced Tilted-Angle Acoustofluidic Chip for Cancer Cell Manipulation, *IEEE Electron*
31 337 *Device Letters*, 2021, **42**, 577–580.
- 32 338 26Y. Chen, M. Wu, L. Ren, J. Liu, P. H. Whitley, L. Wang and T. J. Huang, High-throughput
33 339 acoustic separation of platelets from whole blood, *Lab Chip*, 2016, **16**, 3466–3472.
- 34
35
36
37
38
39
40
41
42
43
44
45
46
47
48
49
50
51
52
53
54
55
56
57
58
59
60

341 **FIGURE LIST**

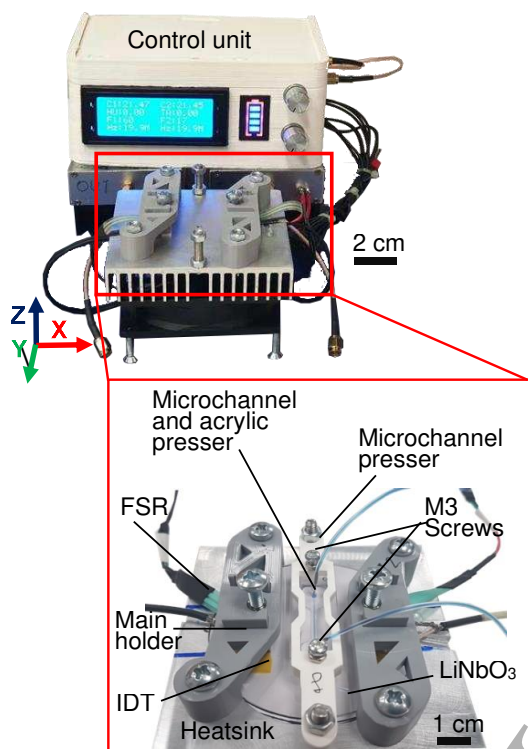
342 (A)



343 (B)

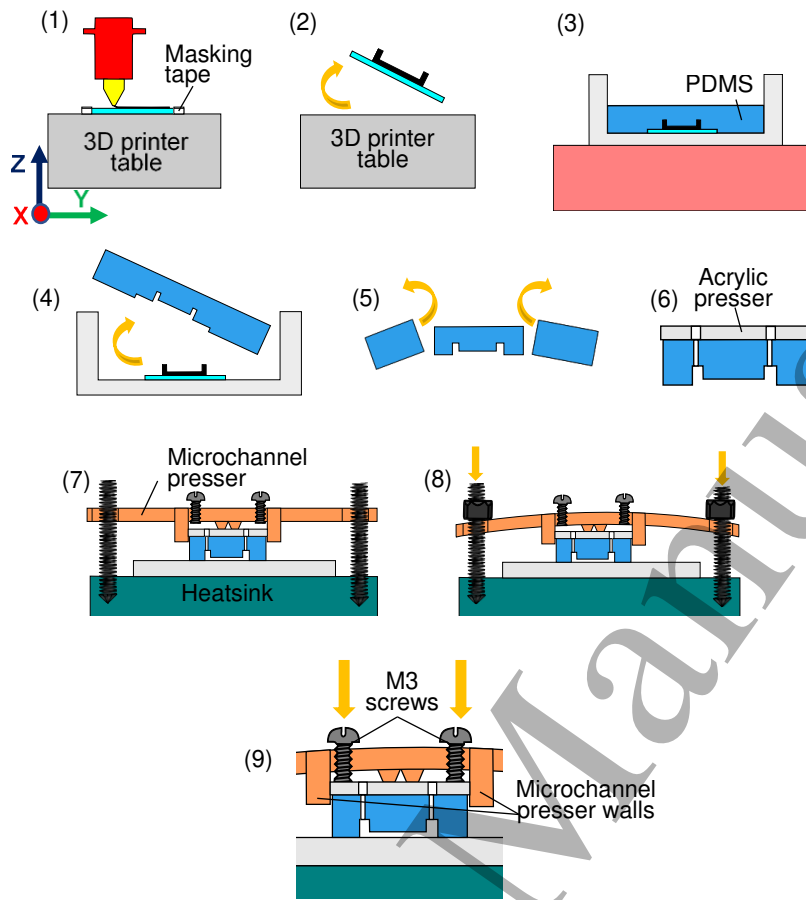


344 (C)

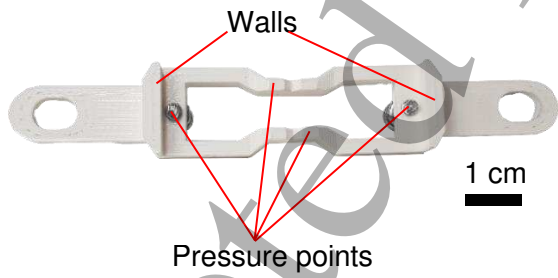


345 (D)

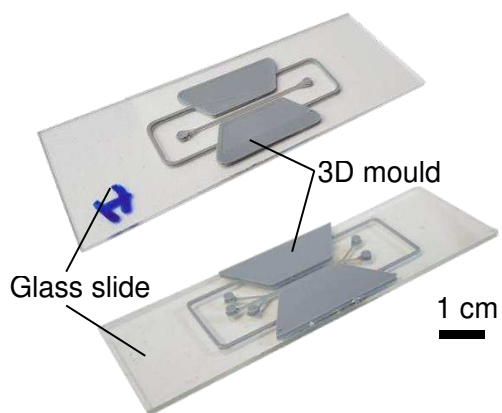
346 **Figure 1.** (A) Real-life flexible printed circuit board (FPCB) pre-patterned with interdigital
 347 electrodes (IDEs) with a zoom inset of the interdigital electrodes. (B) Schematic diagram of the
 348 Versatile Acoustofluidic Device (VAD) and a portable control unit, that can drive a cooling fan
 349 and provide radio frequency (RF) signals to drive the two IDTs. The RF signals are amplified by
 350 two 6W power amplifiers (PA1 and PA2). Each IDT is connected to a matching network (MN1
 351 and MN2) for impedance matching. The values of the capacitor (C) and inductor (L) are 68 pF and
 352 470 nH, respectively. The sensing components include two temperature sensors (T1 and T2) and
 353 force-sensitive resistors (FSR1 and FSR2). (C) 3D exploded view of the VAD with an inset
 354 presenting the assembly and components at the localised pressers. (D) The portable control unit
 355 and the VAD with an inset demonstrating the real-life model of the assembled VAD on the
 356 heatsink.



357 (A)

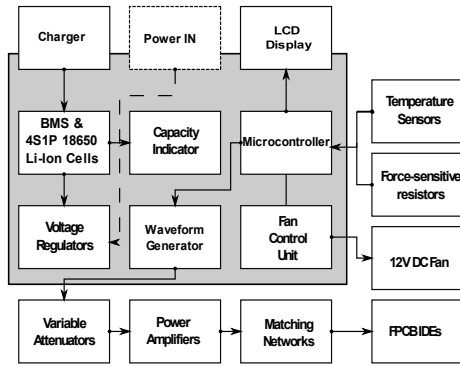


358 (B)



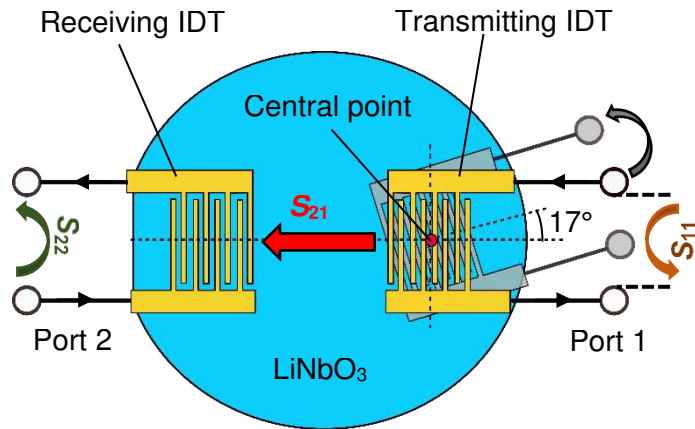
359 (C)

360 **Figure 2.** (A) The development steps of the microchannel using the glass-bottom 3D printed
361 mould. (B) The microchannel presser with its the pressure points and walls highlighted. (C) Real-
362 life models of the glass-bottom 3D printed mould.



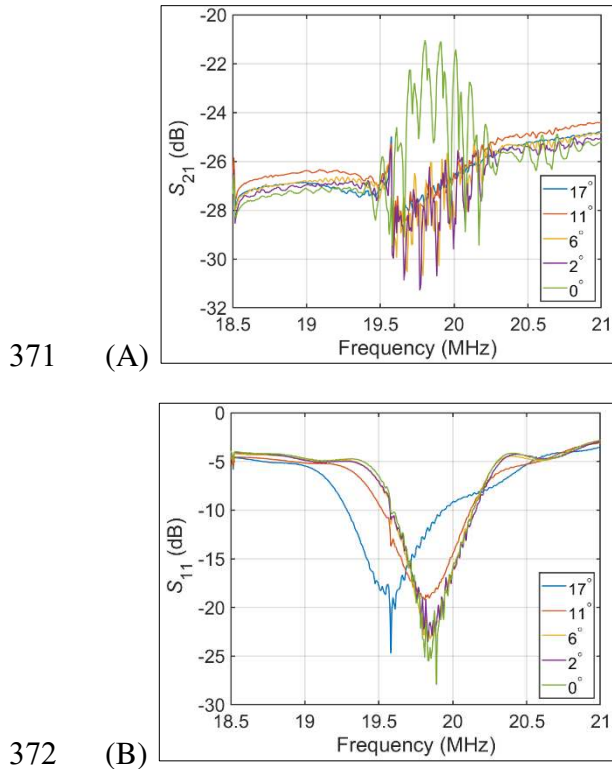
363

364 **Figure 3.** The respective block schematic demonstrating all the internal and external components
 365 of the control unit.
 366

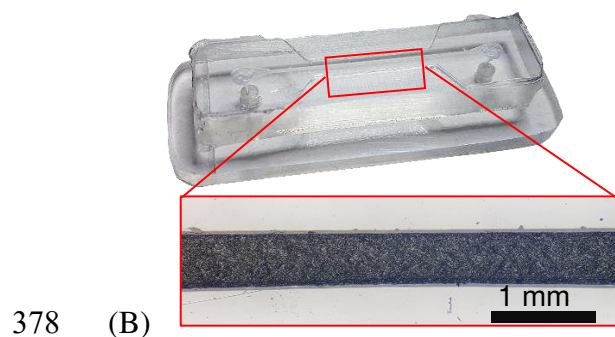
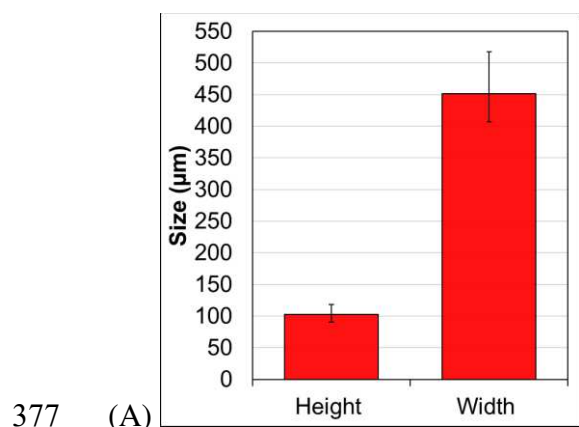


367

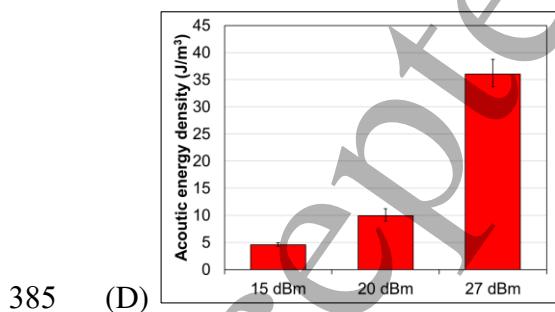
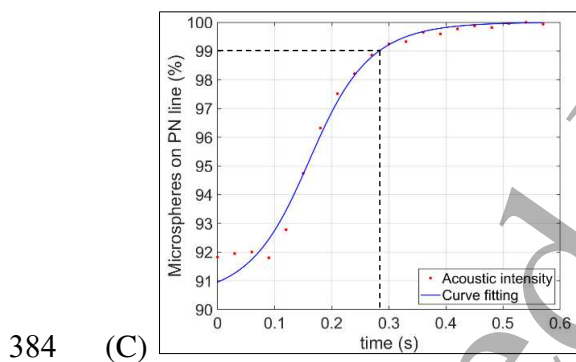
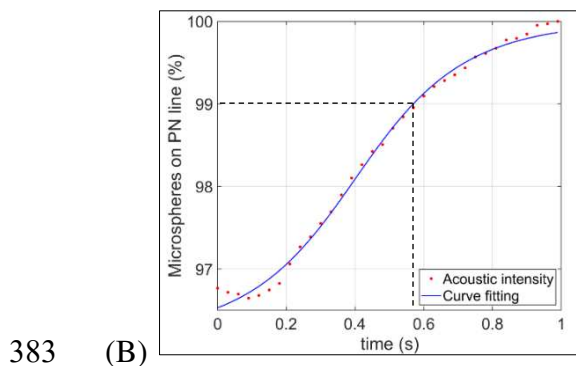
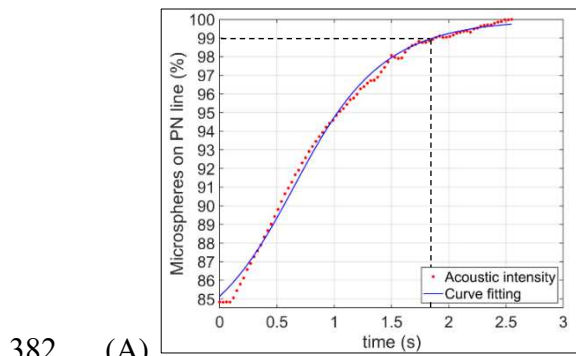
368 **Figure 4.** IDT rotation test for investigating the use of the vector network analyser (VNA) to
 369 register the alignment of the IDTs. The transmitting IDT being rotated around its central point,
 370 while the receiving IDT is held fixed.



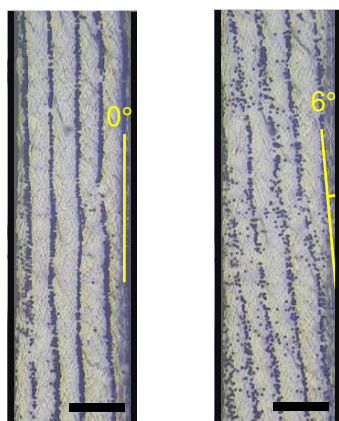
27
28 373 **Figure 5.** S -parameters of the VAD during the rotation of one IDT. (A) Average insertion loss
29 374 (S_{21}) for each different angle during the rotation. (B) Average reflection coefficient (S_{11}) for each
30 375 different angle during the rotation.
31 376



27
28 379 **Figure 6.** (A) The 3D printed mould's average height and width of $102.8 \pm 11.4 \mu\text{m}$ (Mean \pm SD)
29 380 and $451.4 \pm 42.6 \mu\text{m}$ (Mean \pm SD), respectively. (B) Real-life model of a $500 \mu\text{m}$ wide
30 381 microchannel sitting on top of the acrylic presser.



386 **Figure 7.** Acoustic energy density of the VAD with parallel IDTs. (A)-(C) Under the input power
387 of 15 dBm, 20 dBm, and 27 dBm, the time for 99% of microspheres to reach the PN line is ~1.9,
388 ~0.6, and ~0.3 sec, respectively. (D) The average acoustic energy densities for the three input
389 powers are 4.6, 9.9, and 36 J/m³, respectively (n = 3).

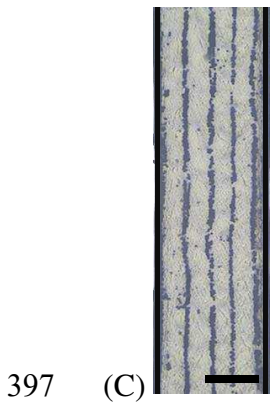
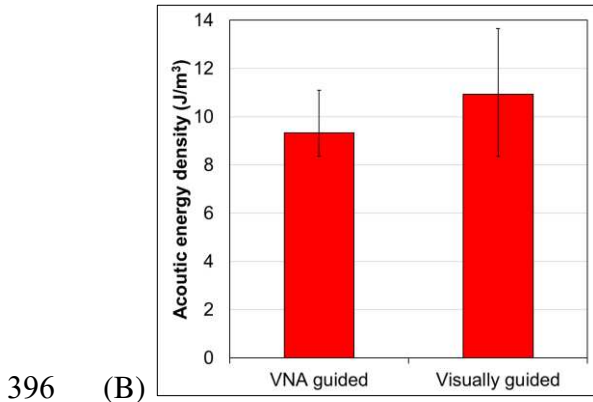
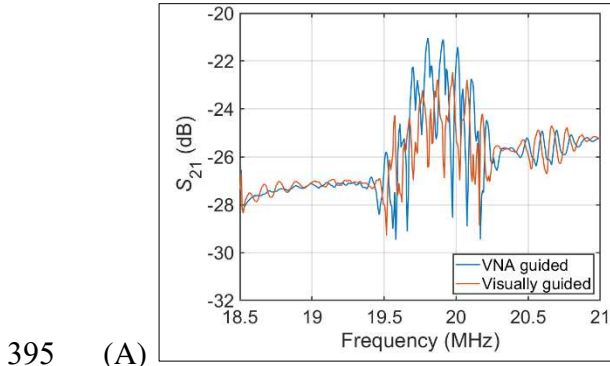


390

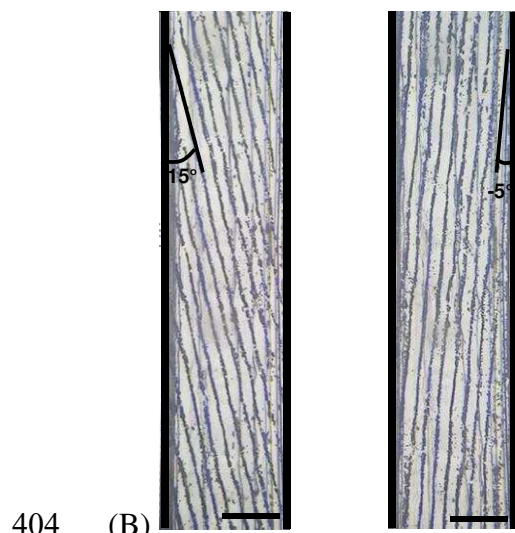
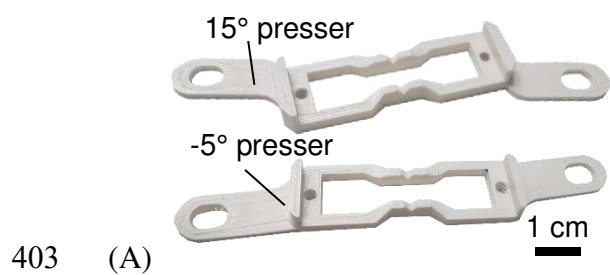
391 (A)

(B)

392 **Figure 8.** Microscope images showing the reconfigurability of the VAD in setting the PN lines to
393 (A) 0° and (B) 6° . The microspheres are aggregated on the PN lines exhibiting the angle against
394 the wall of the microchannel. (200 μm scale bar)



41
42
43 398 **Figure 9.** (A) The S_{21} of the VAD assembled using the VNA and the visually guided assembly of
44 399 the two IDTs. ($n = 5$) (B) Acoustic energy density of the VAD constructed by the two assembly
45 400 methods, VNA and visually, with an acoustic energy of $9.3 \pm 1.2 \text{ J/m}^3$ (Mean \pm SD) and $10.9 \pm$
46 401 2.7 J/m^3 (Mean \pm SD), respectively. ($n = 3$) (C) Microsphere aggregation on the PN lines of the
47 402 VAD constructed by visually guided assembly ($200 \mu\text{m}$ scale bar).



405 **Figure 10.** Rotating the microchannel to a set tilted-angle. (A) 3D printed 15° and -5°
406 microchannel pressers. (B) Aggregated microspheres on the PN lines of 15° (left) and -5° (right)
407 angles, in regard to the microchannel wall (450 μm scale bar).

408